Multi-Instrument Rainfall-Rate Estimation in the Peruvian Central Andes

JAIRO M. VALDIVIA,[a] DANNY E. SCIPIÓN,[b] MARCO MILLA,[c] AND YAMINA SILVA[d]

Instituto Geofísico del Perú, Lima, Peru

(Manuscript received 19 July 2019, in final form 5 August 2020)

ABSTRACT: Agriculture is one of the main economic activities in the Peruvian Andes; rainwater alone irrigates more than 80% of the fields used for agriculture purposes. However, the cloud and rain generation mechanisms in the Andes still remain mostly unknown. In early 2014, the Instituto Geofísico del Perú (IGP) decided to intensify studies in the central Andes to better understand cloud microphysics; the Atmospheric Microphysics And Radiation Laboratory officially started operations in 2015 at IGP's Huancayo Observatory. In this work, a Ka-band cloud profiler [cloud and precipitation profiler (MIRA-35c)], a UHF wind profiler [Clear-Air and Rainfall Estimation (CLAIRE)], and a VHF wind profiler [Boundary Layer and Tropospheric Radar (BLTR)] are used to estimate rainfall rate at different conditions. The height dependence of the drop size diameter versus the terminal velocity, obtained by the radars, in the central Andes (3350 m MSL) was evaluated. The estimates of rainfall rate are validated to ground measurements through a disdrometer [second-generation Particle, Size, and Velocity (PARSIVEL^2)] and two rain gauges. The biases in the cumulative rainfall totals for the PARSIVEL^2, MIRA-35c, and CLAIRE were 18%, 23%, and −32%, respectively, and their respective absolute biases were 19%, 36%, and 63%. These results suggest that a real-time calibration of the radars, MIRA-35c and CLAIRE, is necessary for better estimation of precipitation at the ground. They also show that the correction of the raindrop terminal fall velocity, obtained by separating the vertical wind velocity (BLTR), used in the estimation the raindrop diameter is not sufficient, especially in convective conditions.

KEYWORDS: Atmosphere; South America; Drop size distribution; Radars/Radar observations; Wind profilers; Spectral analysis/models/distribution

1. Introduction

In recent years, natural hazards of hydrometeorological origin have become more frequent in Peru (Martínez Grimaldo et al. 2005). There are scientific and political interests in understanding such events due to their social and economic impact. The complex topography of the Andes, which covers lot of the Peruvian territory, makes it rather challenging to accurately predict amounts of precipitation using satellite observations (Derin et al. 2016; Mourre et al. 2016; Mantas et al. 2015; Scheel et al. 2011). On the other hand, atmospheric models are not able to adequately represent precipitation over complex terrains. Regional numerical models have been used to carry out studies on different mountainous regions, including the Andes (Barrett et al. 2009; Viale and Norte 2009; Junquas et al. 2018), but these models usually overestimate the precipitation as presented by Moya-Álvarez et al. (2018a,b, 2019).

Peru does not have a weather radar network, but there are different initiatives for their future implementation. The complex topography of the Peruvian Andes brings several technical difficulties (e.g., accessibility, electricity, security) that will need to be taken under consideration before such a network could be implemented

Vertically pointing radars obtain information from the atmospheric column above them. Even though they cannot provide spatial distribution, they can clearly show the time evolution of precipitation. Wind profiler radars are usually sensitive to clear-air echoes, but depending on their operational frequency, they can also be sensitive to hydrometeors (e.g., Ralph 1995; McDonald et al. 2004). Under such circumstances, the meteorological radars measure the net effect of the terminal fall speeds of hydrometeors and the motion of air (e.g., Williams et al. 1995). In that case, clear-air processes can generate a bias in the wind estimates. Because of that, a more careful analysis in the spectral domain is required to separate the echoes of clear air and hydrometeors (Williams 2002).

To obtain atmospheric data to study the physical processes associated with water and energy balance, in 2015 the Instituto Geofísico del Perú (IGP) implemented the Atmospheric Microphysics and Radiation Laboratory (LAMAR) at the Huancayo Observatory (12.0°S, 75.3°W, 3313 m MSL). LAMAR is composed of a unique set of instruments for atmospheric studies and the validation of atmospheric models in the Peruvian central Andes: a VHF Boundary Layer and Tropospheric Radar (BLTR) was updated in 2015; a Ka-band cloud profiler [cloud and precipitation profiler (MIRA-35c)] was installed in late 2015 for cloud and rainfall estimation; a disdrometer [second-generation Particle, Size, and Velocity (PARSIVEL^2)]; a few rain gauges. LAMAR also served as a testing site for the new UHF wind profiler [Clear-Air and Rainfall Estimation (CLAIRE)] radar that was fully designed and constructed at IGP's technological development facility, the Jicamarca Radio Observatory (JRO) (Oscanoa et al. 2016). CLAIRE was designed to operate at 445 MHz, which makes it sensitive to turbulence and

[a] ORCID: 0000-0003-0709-1163.
[b] ORCID: 0000-0002-6807-0238.
[c] ORCID: 0000-0001-9067-863X.
[d] ORCID: 0000-0003-0653-0224.

Corresponding author: Danny E. Scipión, dscipion@igp.gob.pe

DOI: 10.1175/JTECH-D-19-0105.1

precipitation. This particular set of instruments at LAMAR allowed the study of precipitation at different radar frequencies and for different scattering mechanisms, and it aims to evaluate the performance of satellite in precipitation retrievals like the Global Precipitation Measurement (GPM; Hou et al. 2014).

In typical radar meteorology applications, the radar reflectivity Z is converted to rainfall intensity using a power-law relationship in the form of $R = aZ^b$ (Marshal and Palmer 1948). The error of the R–Z relationship depends on both the reflectivity measurement uncertainty and the error caused by the empirical determination of the coefficients of the power-law relationship. Different types of hydrometeors and different types of precipitation systems requires their own power-law relationship. The real relationship between the radar reflectivity and rainfall rate depends on the structure of the drop size distribution. The advantage of using profiler radars is that the measured Doppler spectra can be transformed into number concentration versus drop size through the relationship between drop size (D) and terminal fall velocity (w_t), as empirically suggested by Atlas et al. (1973). This relationship was formulated based on the measurements of Gunn and Kinzer (1949). Beard (1977) proposed a similar relationship through simulations. The air density (ρ) plays an important role in the terminal fall velocity, Foote and Du Toit (1969) found the relationship $w_t \propto \rho^{0.4}$. A polynomial approximation for the height dependence of the air density, assuming U.S. standard atmosphere conditions, have been used in several studies (Peters et al. 2002, 2005, 2010; Das et al. 2010, 2011a,b; Das and Maitra 2016). Bringi et al. (2018) analyzed the fit equation of Gunn and Kinzer (1949) data with the height dependence proposed by Foote and Du Toit (1969) at 212 and 1400 m MSL. Bringi et al. (2018) results indicate that under light to moderate wind gusts, the mean fall speeds agree well with fits to the terminal velocity measured in the laboratory by Gunn and Kinzer (1949) from 100 μm up to precipitation sizes. However, previous studies that evaluate D–w_t relationship over high-altitude areas such as the Andes do not exist; it will be evaluated in this study.

Drop size distribution (DSD) parameters derived from Doppler spectra are under the assumption of stagnant air (i.e., $w = 0$). However, vertical winds can bias the Doppler spectra of vertically pointing radars and their retrieved parameters, resulting in precipitation mismatch with disdrometer retrievals at the ground. In the same way, turbulence and wind shear can bias the D–w_t relationship by broadening the spectrum (Atlas 1964). Peters et al. (2002) found a correlation coefficient $r = 0.87$ in the comparison between vertically pointing micro radar and rain gauges and 5% bias in the total rainfall, near to sea level. Valdivia (2018) tested the Peters et al. (2002) methodology applied to MIRA-35c, which does not include wind correction in LAMAR facilities; 59 identified rain events were evaluated, and a bias of 10% and a standard error of 2.8 mm were found. By modeling the effect of the vertical wind, Peters et al. (2005) found that a bias of $\pm 0.5\ \mathrm{m\,s^{-1}}$ can cause precipitation errors as high as 100%.

Simultaneous measurements of vertical wind velocity and drop size distribution would allow a more accurate rainfall-rate estimates. Different radar-based methods have been proposed for the retrieval of vertical wind speeds (w) and DSD, like the dual-frequency method (e.g., wind radar and rain radar; Williams 2002; Schafer et al. 2002) and Mie notch retrieval (Lhermitte 1988).

The wind profilers are limited by the low sensibility and large beamwidth, which lead to coarse temporal and range resolutions and to an increase in errors because of turbulence and wind shear during strong convective rain events (Schafer et al. 2002). Kollias et al. (2002) and Firda et al. (1999) demonstrate that under precipitating conditions, the oscillations observed in the Doppler spectra at 94 GHz can be used as reference points for the retrieval of the vertical air motion. Combined with centimeter-wavelength radars, 94 GHz radars can provide high spatial and temporal resolution in stratiform and convective rain (Kollias et al. 2003, 2007; Giangrande et al. 2012). However, they are limited to moderate rainfall cases where large enough drops are presented in order to produce significant non-Rayleigh scattering signatures (Mie notch in the Doppler spectra). Moreover, the concentration parameter and the rain rate can be highly uncertain due to strong attenuation of cloud radar signals in rain (Tridon et al. 2017). A new multi-frequency technique has shown potential for estimating DSD using a combination of the observed radar Doppler spectra at Ka and W bands (Tridon and Battaglia 2015; Tridon et al. 2017). Using this technique, the spectral matching and their differences can be used to correct the differential attenuation, the effects of miscalibration, or air state parameters, such as vertical wind and broadening caused by turbulence and wind shear. Kneifel et al. (2016) and Tridon et al. (2019) extended the concept of dual frequency to triple frequency to provide new opportunities for ice and liquid retrievals.

Dual- and triple-wavelength radar observations require matched sampling volumes and equal temporal resolutions to target the same precipitation microphysics. Additionally, a sufficient number of samples and high signal-to-noise ratios (SNR) are needed in order to reduce errors in radar reflectivity measurements for all the radars (Williams and Vivekanandan 2007; Pfitzenmaier et al. 2019). In millimeter-wavelength radars different antenna sizes or subilluminations of the reflector by the higher-frequency radar system are needed in order to match sampling volumes and obtain high spatial resolutions (Ellis and Vivekanandan 2011; Kollias et al. 2014).

The application of novel techniques using our current radar systems is difficult because of their different specifications (see Table 1). Due to sampling mismatches and different temporal resolutions, a different spectral broadening effect is expected, which might be impossible to remove from our current radar dataset. Correcting these errors will form the bases for future work.

In this study, we assessed the relationship between drop size and terminal fall velocity at 3300 m MSL in the central Andes. We use multiple instruments in order to evaluate their abilities to estimate the rainfall rate, as well as the advantages and disadvantages of each. We evaluate the performance of our radars individually to estimate rainfall rate, and we use a combination of radar observations (clear air and precipitation) in order to reduce the uncertainty generated by the relationship between drop diameter and terminal fall velocity. The paper is organized as follows: a description of the instrumentation is presented in section 2; the methodology is described in

TABLE 1. Radar specifications.

Specification	MIRA-35c	CLAIRE	BLTR
Operation frequency	34.85 GHz	445 MHz	49.92 MHz
Transmission power	Magnetron 2.5 kW	Solid state 5 kW	Solid state 30 kW
Antenna	1-m diameter Cassegrain	Phase array (1 Tx, 3 Rx)	Phase array (3 Rx)
Beamwidth	0.6°	9.46°	19.79°
No. of range gates	415	67	132
Range resolution	31 m	75 m	75 m
Range	0.15–13 km	0.52–6 km	0.22–10 km
Nyquist velocity range	10.34 m s^{-1}	14.04 m s^{-1}	11.74 m s^{-1}
No. of spectral bins	128	256	256
Spectral resolution	16.16 cm s^{-1}	10.97 cm s^{-1}	9.17 cm s^{-1}
Temporal resolution	5.6 s	23.0 s	32.8 s

section 3; results are presented in section 4; conclusions are outlined in section 5.

2. Instrumentation

Measurements for the present study have been made at IGP's Huancayo Observatory (12°02′18″S, 75°39′22″W) at 3330 m MSL, which is located 20 km from the center of the city of Huancayo (Fig. 1), where the LAMAR was set up. Annual rainfall climatology at this location is 700 mm, and it is characterized as being dry in winter (austral) and rainy in summer (with maximum precipitation in February). According to Köppen–Geiger classification (Peel et al. 2007), Mantaro valley has an arid cold steppe climate.

LAMAR consists of a collection of instruments for atmospheric studies in the central part of the Peruvian Andes. LAMAR's instruments used in this work are presented in Fig. 2: (Fig. 2a) CLAIRE radar, (Fig. 2b) MIRA-35c radar, (Fig. 2c) BLTR, and (Fig. 2d) optical disdrometer (PARSIVEL^2). We also include a couple of tipping-bucket rain gauges for the analysis. All these instruments are relatively close to each other (less than 50 m), except for BLTR and a rain gauge, which are separated 170 and 200 m from the rest, respectively. The instruments are described below.

a. MIRA-35c radar

The MIRA-35c is a high-frequency cloud profiler radar. The system design includes a 1-m-diameter dish antenna. Further details of the system are listed in Table 1. Even when the system is mainly designed for cloud studies, it is also sensitive to precipitation. As is the same with CLAIRE, the spectral analysis of the data finally allows us to estimate rainfall rate (R) after correcting for Mie scattering cross section (Bohren and Huffman 1998).

MIRA-35c, manufactured by Meteorologische Messtechnik GmbH (METEK), is a vertically pointing pulsed radar operating a frequency of 34.85 GHz (λ = 8.6 mm). It uses a magnetron providing 2.5-kW pulse power and transmits a linear polarized signal, while co- and cross-polarized signals are received simultaneously in order to detect Doppler spectra within its Nyquist velocity of $\pm$10.3 m s^{-1}. The system has a vertical range resolution of 31 m, covering a range between 150 m and 13 km above ground, but ranges below to 250 m has been discarded because they are contaminated by ground

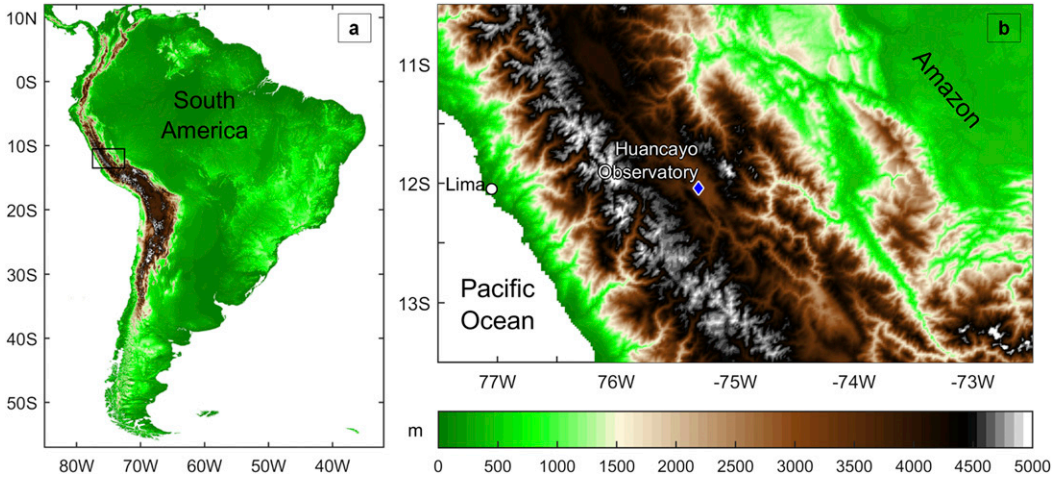

FIG. 1. Location of the IGP's Huancayo Observatory. (a) The observatory is located in South America (12.04°S, 75.32°W) (b) at 3313 m MSL in the central Andes.

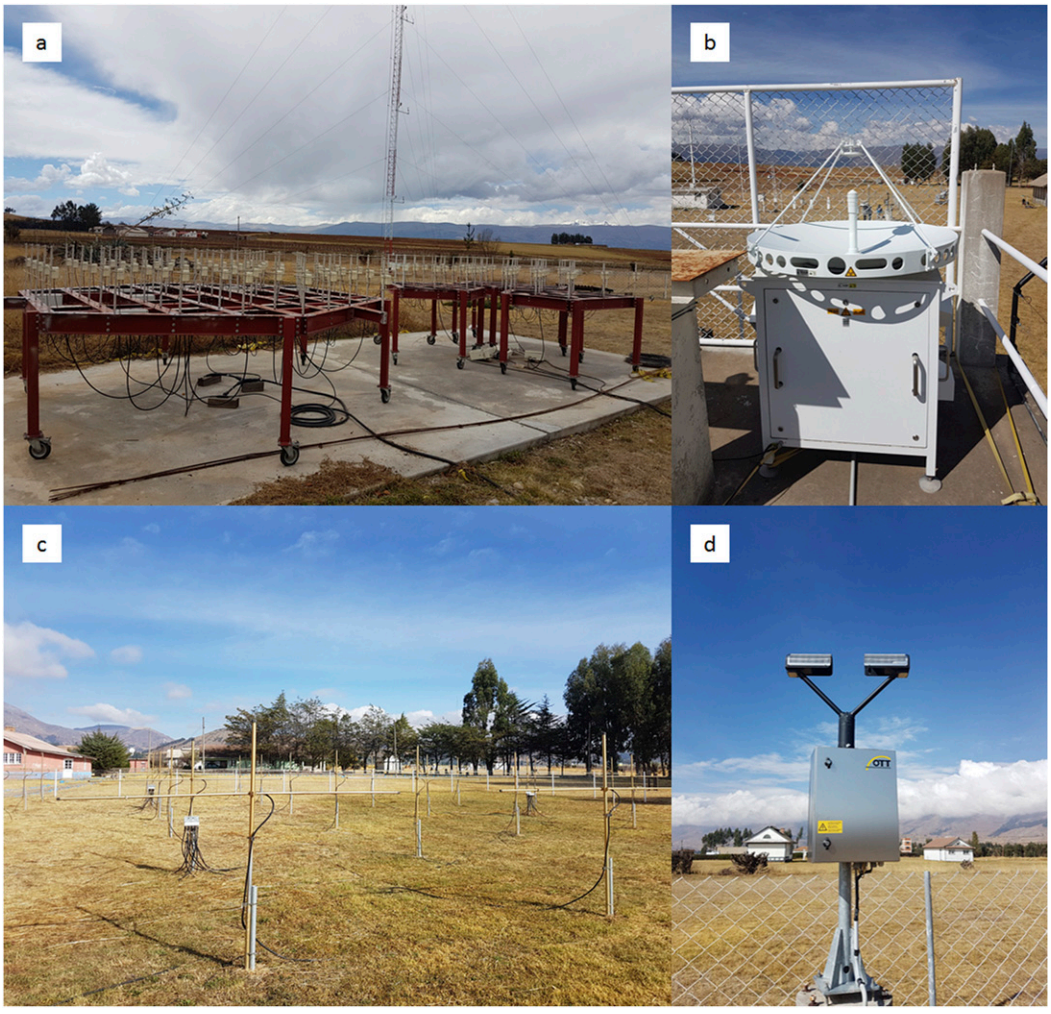

FIG. 2. Atmospheric Microphysics and Radiation Laboratory (LAMAR) instrumentation used in the current study: (a) Clear-Air and Rainfall Estimation (CLAIRE) radar, (b) cloud and precipitation profiler (MIRA-35c) radar, (c) Boundary Layer and Troposphere Radar (BLTR), and (d) optical disdrometer PARSIVEL^2.

clutter. The software of MIRA-35c already includes the standard integral parameters of rainfall within its products; however, in this work just the Doppler spectra will be used. The design of the MIRA-35c energy system includes batteries, a solar panel, and a generator set in addition to the connection to the main power line. This particular combination of power sources makes the system autonomous and stable. Additionally, the transmitter power is recorded at every pulse, which allows to have an accurate radar calibration constant.

b. CLAIRE radar

CLAIRE was designed for turbulence and precipitation studies (Oscanoa et al. 2016). It is a 445 MHz ($\lambda = 0.67$ m) quasi-monostatic radar that consists of one transmitting antenna and three receiving antenna arrays. Due to its operational frequency, it is sensitive to clear-air and precipitation echoes. Three-dimensional wind components are estimated from the turbulence echoes by using the full spectral analysis (FSA; Briggs and Vincent 1992), and rainfall-rate estimations are obtained from hydrometeors. Further details can be found in Table 1. Pulse compression technique (Lewis and Kretschmer 1982) is applied in order to improve the SNR and sensitivity of the clear-air echoes at high ranges. The basic concept of pulse compression is to apply phase modulation on a long transmitted pulse, then demodulate and decode the received signal in order to obtain an equivalent echo sample with much higher peak power, which has significantly better range resolution than an uncoded long transmitted pulse. The system has a vertical range resolution up to 75 m, which covers a range span between 500 m and 8 km above the ground; however, ranges below to 750 m have been discarded because they are contaminated by the coded transmitted pulse. The return signal power of CLAIRE is sensitive to the power line oscillations. Because of its location in the central Andes the Huancayo Observatory is susceptible to power outages caused by thunderstorms, which generates gaps in the radar data and

instabilities in the nominal power. This, in turn, can affect the transmitted nominal power, and ultimately the radar calibration constant. CLAIRE is calibrated by comparing the estimates of precipitation with a more stable system such as the MIRA-35c and PARSIVEL^2. Data obtained during stratiform rain events are used for calibrating CLAIRE because they are less susceptible to attenuation by scattering and absorption mechanisms at the radar frequencies.

The spectral analysis of the signal will allow the discrimination between both clear-air and precipitation echoes by analyzing the characteristic of the distinct vertical velocities. After discriminating the echoes, reflectivities coming only from the hydrometeors are processed in order to obtain fall speed of the particles [$w_t(D)$], the drop size distribution [$N(D)$], liquid water content (LWC), and rainfall rate (R). The methodology for obtaining these parameters is presented in section 3.

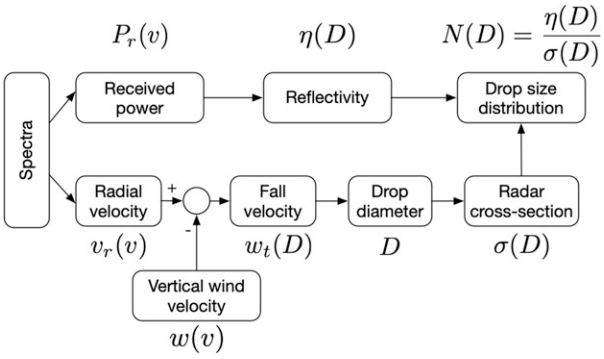

FIG. 3. Flow diagram of the methodology followed to estimate the drop size distribution (DSD) from the radar Doppler spectra. The different steps involve the echoes discriminations between the vertical wind velocity and fall velocity. Procedure is applied to the returned signal of the MIRA-35c and CLAIRE.

c. BLTR

The BLTR was manufactured by Genesis Software Pty Ltd. It is a 49.92 MHz (λ = 6.0 m) monostatic wind profiler radar that consists of three antenna arrays (Fig. 2c). The BLTR operates using the spaced antenna (SA) technique (Briggs 1984), which provides the three components of the winds (zonal, meridional, and vertical) with a vertical resolution of 75 m. Due to its operational frequency, it is mainly sensitive to Bragg scatter mechanisms, but after further processing in the spectral analysis, precipitation echoes were detected during convective precipitation events when large raindrops are observed (as is shown in Fig. 5a). In this study echoes from clear air are processed independently in the spectral domain in order to obtain the true vertical wind component. The BLTR power supply comes directly from the main power line, which makes it vulnerable to problems caused by electrical storms. However, the variations in the power line does not affect the Doppler shift of the observed echoes.

d. Optical disdrometer (PARSIVEL^2)

PARSIVEL^2 is a laser-optical disdrometer that measures the size and velocity of hydrometeors (Löffler-Mang and Joss 2000). The PARSIVEL^2 is a new model of the PARSIVEL, introduced by OTT HydroMet in 2011. PARSIVEL^2 offers improvements over the earlier model. These improvements were evaluated through a comparative study at NASA's Goddard Space Flight Center (Tokay et al. 2014). The PARSIVEL^2 sampling output is 1 min. The raw output provides the number of drops in a 32 × 32 size versus fall velocity matrix. The size range is from 0 to 25 mm, and the class width increases with the size from 0.125 to 3 mm. The first two size classes are left empty due to the low SNR, and the minimum detectable size is approximately 0.25 mm. The fall velocity range is from 0 to 20 m s^{-1}, and the class width increases with fall velocity. The PARSIVEL^2 power supply comes directly from the main power line.

e. Rain gauges

Both rain gauges consist of a tipping bucket with 0.254 mm of accuracy. One of them was manufactured by Texas Electronics (model TE525), and the other manufactured by HS Hyquest Solutions (model CS700). Each tip is recorded for the gauges and the accumulated precipitation is integrated to 1 min values. The rain gauge CS700 is used as a reference for this study, and it has a backup battery that keeps the instrument under continuous operation, even through electrical blackouts. The TE525 rain gauge is located 200 m from the CS700 and is powered only by the main power line.

Further description of the PARSIVEL^2, the rain gauges instrumentation, and their datasets can be found in Valdivia et al. (2020).

3. Methodology

The methodology developed in this study is based on the radar Doppler spectrum, which is used to estimate radar reflectivity and radial velocities. The main objective is to discriminate clear-air echoes and hydrometeors from the measured spectrum. The flow diagram for computing DSD and integral rain parameters is shown in Fig. 3. First, echoes from different scattering mechanisms are separated (for CLAIRE and BLTR), then the hydrometeors fall velocity is corrected using the true vertical wind velocity, and finally, the DSD and rain parameters are computed (Peters et al. 2005, 2010; Maahn and Kollias 2012; Das and Maitra 2016).

a. Echo separation

The echo separation procedure is applied to the radar spectra when different scattering mechanisms are present. This technique consists in identifying multiple peaks in the spectra. There are three spectral peak regimes: single peak, subpeak, separate peak (Williams et al. 2018, Fig. 13). The peaks are determined when the signal is greater than the noise threshold, thus, every valid group of spectral points has at least a single peak. A separate peak is observed when there is another group of spectral points above the noise threshold. Therefore, it is necessary to separate this second peak from the first single peak. Subpeaks are within integration limits of the single peak. Williams et al. (2018) used a valley of at least 6 dB to determinate subpeaks. The subpeak identification will not be applied in this study because scatters from hydrometeors and

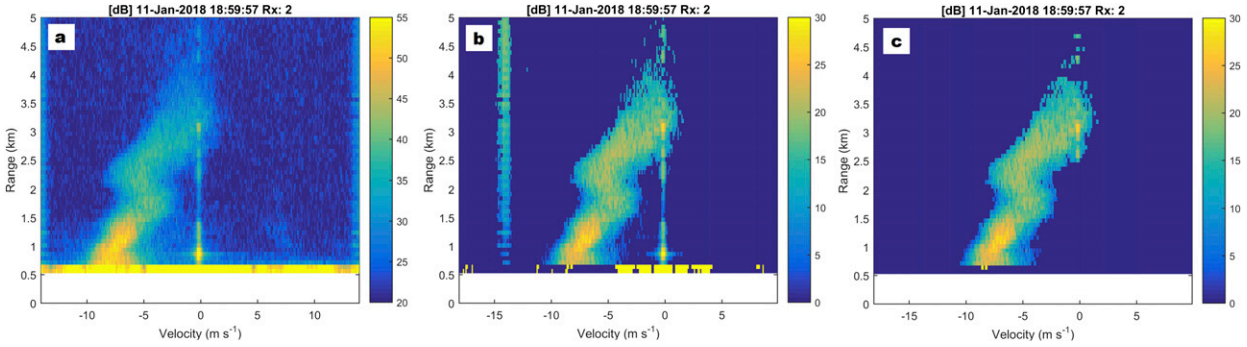

FIG. 4. Ground clutter and interference removal algorithms applied to CLAIRE's spectra: (a) original spectra, (b) spectra shifting, and (c) clean spectra.

the clear-air echoes have different vertical velocities, and as a consequence, their echoes always appear as separate peaks.

1) NOISE REMOVAL

The noise level is not constant at each time step and each range, and it is estimated using Hildebrand and Sekhon (1974) algorithm, which sorts out each single Doppler spectrum by amplitude and removes the largest values of spectral peaks until the following condition is fulfilled:

$$E^2/V \geq n, \tag{1}$$

with E the average of the spectrum, V the variance, and n is the number of temporal averaged spectra, which is referred as incoherent averaging (Welch 1967). The bin, at which the loop stops, is identified as the noise level, which is subtracted from the observed Doppler spectrum for further analysis.

2) SPECTRUM DEALIASING

It is important that the single peak spectra points remain close together to make a proper peak identification; therefore, the velocity folding (aliasing) should be corrected before any additional calculations. The velocity aliasing occurs when the Doppler velocity exceeds the Nyquist velocity boundaries (10.34, 14.04, and 11.74 m s^{-1} for MIRA-35c, CLAIRE, and BLTR, respectively). To correct the velocity aliasing, we limited the upward velocity range to 7 m s^{-1} (except for CLAIRE which is limited to 10 m s^{-1}), and the higher velocity bins are shifted to the other side of the spectrum increasing the downward velocity range (spectra shifting—see Fig. 4b).

After the noise removal and the spectra dealiasing, each spectrum with consecutive spectral points spanning at least 0.5 m s^{-1} above the noise threshold will have a single peak.

In some cases, the spectrum from a single peak appears to be discontinuous due to noisy spectrum, and this will generate an error in the integration limits. To avoid that, spectral points that are not more than 0.45 m s^{-1} of the integration limits are considered as part of the single peak. The values 0.5 and 0.45 m s^{-1} (velocity thresholds) have been adapted to our data from Williams et al. (2018) method.

Once the peaks are found for each range gate, we group the peaks of different range gates in order to avoid combining different echo types (i.e., precipitation, wind, ground clutter) and to classify them properly. Figure 4c shows the group of rain peaks for a specific dwell time, while Fig. 5b shows the groups

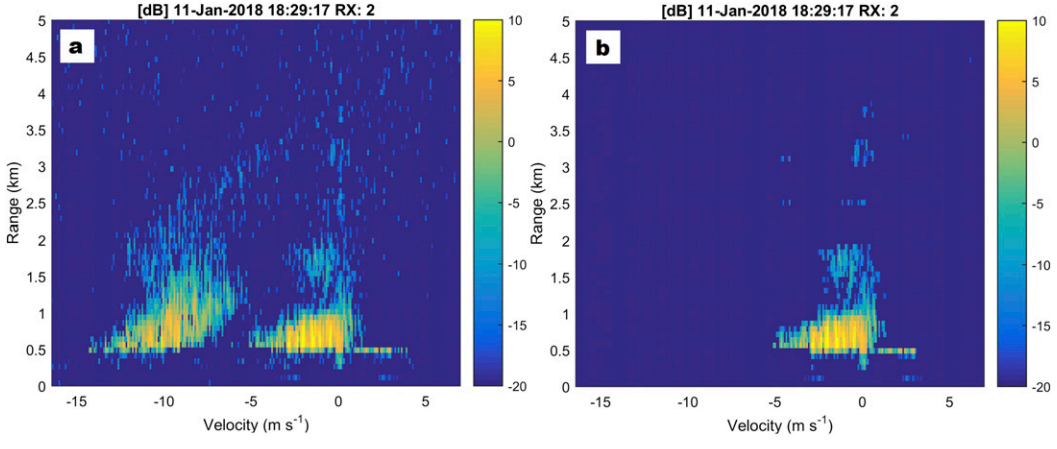

FIG. 5. Echo separation methodology applied to the raw BLTR spectra. (a) Original BLTR spectra where both precipitation and clear-air echoes are observed. (b) Final spectra after precipitation echoes were removed.

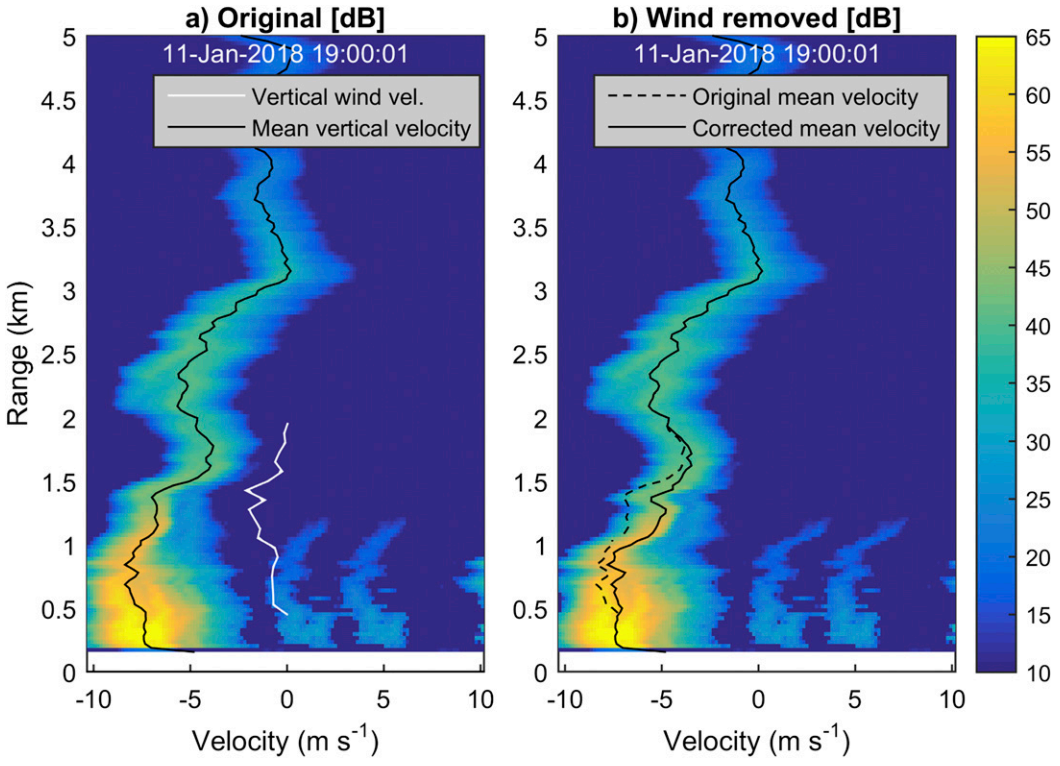

FIG. 6. MIRA-35c rain drop terminal velocity after correcting for wind vertical velocity (white line) obtained from the BLTR after echo separation. The black lines represent the final mean vertical velocity. (a) The original spectra without vertical velocity correction. (b) Spectra with raindrop terminal velocity correction. The black dashed line in (b) indicates the original mean velocity.

of wind peaks. This step allow us to filter vertical interference in the Doppler spectra (see Figs. 4b,c). The group of peaks should meet the following characteristics:

1) r_n is a peak in the range gate n and r_{n+1} is a peak in the range gate $n + 1$; they are part of the same group of peaks, if the peak r_{n+1} has a mean radial velocity within the boundaries of the peak r_n.
2) If the group of peaks have similar radial velocities (i.e., $\mathrm{RMS}(v_r) \leq 0.2\,\mathrm{m\,s^{-1}}$) and is larger than 1/3 of the all range gates number, the group of peaks are flagged as interference (and/or clutter) and they are discarded.
3) If the radial velocity of the nearest peak to surface of the group of peaks is less than $-5\,\mathrm{m\,s^{-1}}$, this is flagged as rain echo, else, as clear-air echo.

This procedure is applied to CLAIRE and BLTR because they both are sensitive to two scattering mechanisms, and they present more than just a single precipitation peak. Separation of clutter and interference from the single precipitation peak for CLAIRE is presented in Fig. 4, while the echo discrimination between clear air and precipitation for the BLTR is presented in Fig. 5.

b. Computation of rainfall parameters

The DSD is expressed as the number of drops per volume of air for a given drop size interval $N(D)$. From the Doppler spectra, the DSD is estimated, then the other rainfall parameters are calculated based on DSD.

The spectral volume backscattering cross section $\eta(v, r)$ ($\mathrm{m^{-1}\,s}$) at the Doppler velocity v and the range gate centered at r is related to the received spectral power $P_r(v, r)$, received by the radar, by

$$\eta(v,r)dv = p(v,r)dv\,C\,r^2, \tag{2}$$

where C is the radar calibration constant containing radar specific parameters, and includes information like transmit power and antenna gain.

We include the conventional weather radar terminology the "equivalent spectral radar reflectivity factor,"

$$Z_e = \frac{\int \eta(v)\,dv}{\left(\frac{\pi^5}{\lambda^4}\right)|K|^2}, \tag{3}$$

with $|K^2| \approx 0.93$. Within the Rayleigh approximation ($D \ll \lambda$), Z_e is the usual radar reflectivity factor Z, defined in Eq. (12).

The Doppler spectrum can be characterized based on its first and second moments, which correspond to the Doppler radial velocity and the Doppler spectrum width, respectively.

In the case of vertical pointing radars, the Doppler spectrum width is the sum of the individual contributions of different

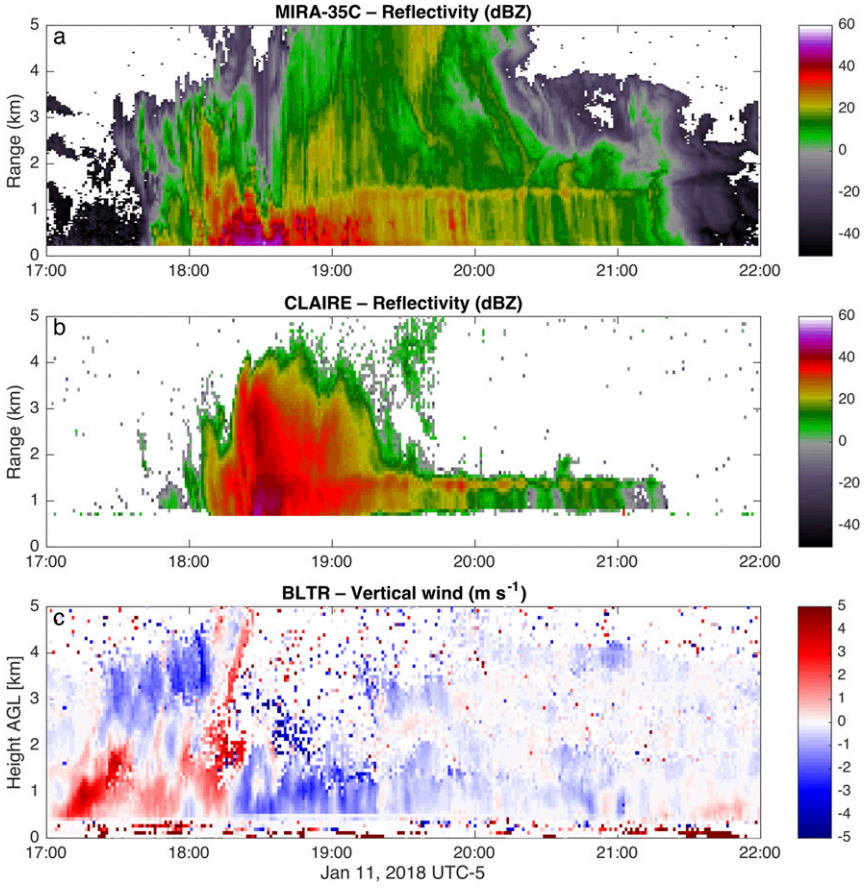

FIG. 7. Rain event of 11 Jan 2018. (a) Radar reflectivity factor (MIRA-35c). (b) Radar reflectivity factor (CLAIRE). (c) Vertical wind velocity (BLTR). The differences between the radar reflectivity observed by the different radars are due to the backscatter attenuation observed at different radar frequencies. MIRA-35c is more sensitive to clouds, but more sensitive to attenuation due to strong precipitation. Meanwhile, CLAIRE is less sensitive to cloud echoes and to attenuation during strong events. The melting layer in both systems is detected at approximately 1.5 km AGL. The range gate closest to the ground is identified at 250 m for MIRA-35c, 750 m for CLAIRE, and 500 m for BLTR.

mechanisms, like shear, different speeds of fall for different size hydrometeors, change in orientation or vibration of hydrometeors, and turbulence. Due to the separation of the scattering mechanisms, only the spectrum width caused by different speeds of fall for different size hydrometeors is analyzed in detail are considered in this study. The spectral broadening measured by wind profilers is not analyzed because the high uncertainty caused by the sampling volume mismatch and temporal resolutions.

The Doppler velocity v_r ($\mathrm{m\,s^{-1}}$) is the sum of the terminal fall velocity of drop w_t the mean airflow velocity w and the turbulent flow velocity σ_w, as described below (Bezvesilniy et al. 2013):

$$v_r = w_t + w + \sigma_w. \tag{4}$$

Turbulent flow velocity σ_w is a random variable characterized by a zero-mean Gaussian distribution (Atlas et al. 1973; Doviak and Zrnić 1984).

Estimation of the terminal velocity of hydrometeors is presented in Fig. 6, where the separation of the vertical wind component is performed to the measured radial velocity: (Fig. 6a) Doppler spectra measured by MIRA-35c, the white line represents the mean wind vertical velocity measured by BLTR; and (Fig. 6b) spectra after the rain drop terminal velocity correction. The black line indicates the mean Doppler velocity, and the black dashed line, the mean measured Doppler velocity.

The raindrop terminal fall velocity w_t can be related to the diameter of falling drops D (Gunn and Kinzer 1949) by

$$D(w_t, z) = \frac{1}{0.6}\ln\left[\frac{10.3}{9.65 - w_t/\delta(z)}\right]. \tag{5}$$

The height dependence of the terminal velocity due to change in air density $\delta(z)$ is the Atlas et al. (1973) second-order polynomial approximation of Foote and Du Toit (1969), given by

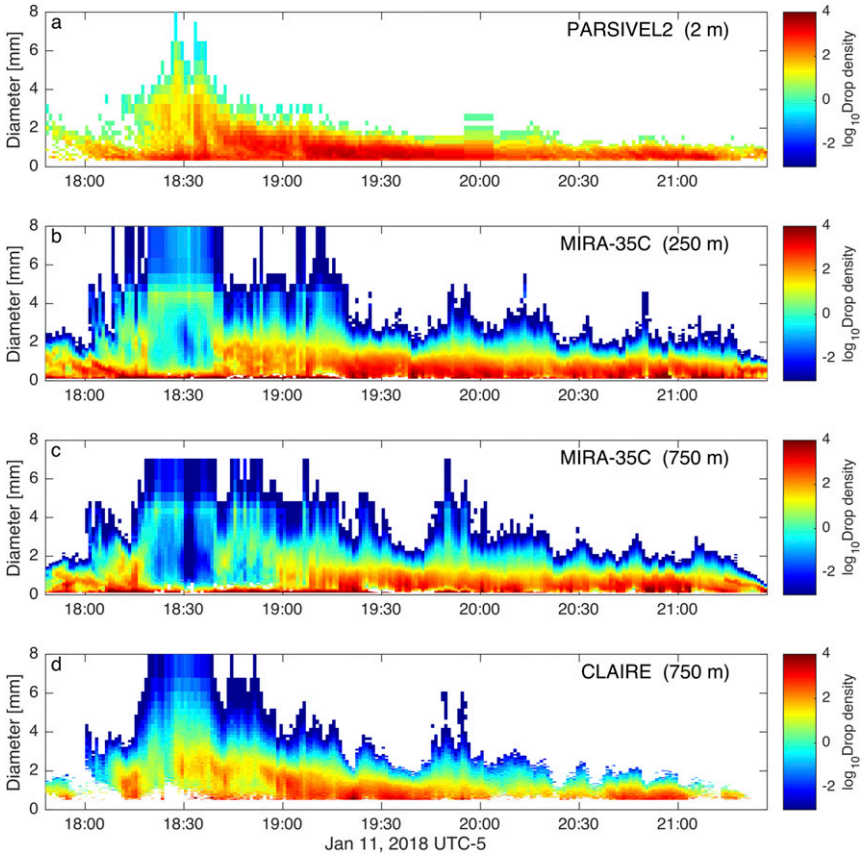

FIG. 8. Drop size distribution retrieval for the rain event of 11 Jan 2018 from different instruments. (a) PARSIVEL^2 at 2 m, (b) MIRA-35c at 250 m, (c) MIRA-35c at 750 m, and (d) CLAIRE at 750 m. Radar retrievals are obtained at the closest ranges to surface. The "spurious mode" can be clearly observed in the MIRA-35c in (b) between 1820 and 1840 LT around 4.5 mm of diameter; it is caused by the first minimum in the backscattering cross sections (Mie notch) at 35 GHz.

$$\delta(z) = (1 + 3.68 \times 10^{-5} z + 1.71 \times 10^{-9} z^2), \tag{6}$$

where the elevation z is related to r and the radar altitude z_0 (3.3 km MSL) by $z = r + z_0$. Equation (5) is applied only in the size range $D \geq 0.16$ mm and $w_t \delta(z) \leq 9.6\ \mathrm{m\ s^{-1}}$.

Therefore, the spectral volume scattering cross section can be obtained in the Doppler velocity domain as

$$\eta(D, z) = \eta(v, z) \frac{\partial v}{\partial D(v, z)}, \tag{7}$$

where $\partial v / \partial D = 6.18 \exp(-0.6\ \mathrm{mm}) \delta(z)$ is derived from Eq. (5).

Dividing $\eta(D, z)$ by the single backscattering cross section $\sigma(D)$ of a raindrop of diameter D yields the drop size distribution

$$N(D, z) = \frac{\eta(D, z)}{\sigma(D)}. \tag{8}$$

The single particle backscattering cross section $\sigma(D)$ of a sphere with diameter D could be expressed analytically using the Rayleigh approximation at 445 MHz,

$$\sigma(D) = \frac{\pi^5}{\lambda^4} |K|^2 D^6, \tag{9}$$

where the drop diameter are small compared to the wavelength. At 35 GHz, $\sigma(D)$ is calculated using Mie scattering theory (Bohren and Huffman 1998). The diameter is defined here as the volume equivalent sphere diameter: $D = (6V/\pi)^{1/3}$, where V is the volume of the drop.

At 35 GHz the rain attenuation is very severe, especially at high rain rate. Gaseous attenuation, on the other hand, can be negligible due to small pathlength in the lower troposphere. Therefore, the rain attenuation correction is applied using a recursive algorithm to MIRA-35c data. We estimate the attenuation coefficient κ_r ($\mathrm{m^{-1}}$) from the drop size distribution by

$$\kappa_r = \int \sigma_e(D) N(D)\, dD, \tag{10}$$

where σ_e is the single particle extinction cross section. The rain attenuation coefficient is related to the two way attenuation (A) in the next range gate by

$$A(z_2) = \exp[-2\kappa_r(z_1)\Delta z]. \quad (11)$$

In this technique, all parameters in the lowest range gate are assumed to have zero rain attenuation.

Other rain parameters like rainfall rate, radar reflectivity, and liquid water content are obtained based on the estimates of the DSD (Bringi and Chandrasekar 2001). The radar reflectivity factor ($mm^6\,m^{-3}$) is defined by

$$Z = \int N(D)D^6\,dD. \quad (12)$$

The liquid water content ($g\,m^{-3}$)

$$\mathrm{LWC} = \rho_w(\pi/6)\int N(D)D^3\,dD \quad (13)$$

with the density of water $\rho_w = 1\,g\,cm^{-3}$ and the rain rate ($mm\,h^{-1}$)

$$R = (6\times10^5\times\pi)\int N(D)w_t(D)D^3dD \quad (14)$$

are calculated. The reflectivity factor measured by MIRA-35c and CLAIRE, and vertical wind velocity measured by BLTR (after the echo separation) are shown in Fig. 7 for a rain event of 11 January 2018. Note that the valid heights closest to the surface are 250 m for MIRA35c, 750 m for CLAIRE, and 500 m for BLTR.

In the case of the PARSIVEL^2 disdrometer, the raw output is the number of drops at the ith size and jth velocity bin ($C_{i,j}$) and DSD is calculated as

$$N(D) = \frac{1}{\mathrm{Time}}\sum_{i=1}^{n}\sum_{j=1}^{m}\frac{C_{i,j}}{w_{t_j}\mathrm{Area}(D_i)\Delta D_i}, \quad (15)$$

where ΔD_i is the width of the ith size bin; and n and m are the size and velocity bins, respectively, and both are equal to 32. Area (D_i), the effective disdrometer sampling area is calculating considering partially detected drops across PARSIVEL^2's laser sheet and is equal to 180 mm × (30 mm − D_i/2). w_{t_j} is the measured raindrop fall speed at the jth velocity bin.

An example of drop size distribution retrieval of MIRA-35c, CLAIRE, and PARSIVEL^2, for a rain event of 11 January 2018, is shown in Fig. 8. The rain rate and reflectivity derived from the drop size distribution for the same event is presented in Fig. 9.

c. *Rainfall statistics*

We compared the precipitation estimates of the different instruments (radars, disdrometers, and rain gauges). Rainfall events were collected during the rainy season of 2018 (January–March 2018), there were identified 26 events where the rain total exceed 1 mm. A rainfall event is defined following Tokay et al. (2014), as a rain period separated by 2 h or longer rain-free periods in the rain-rate time series of the PARSIVEL^2, and a rain/no-rain threshold was set to a minimum of 10 drops and a rain rate of 0.1 $mm\,h^{-1}$. Unfortunately, not all instruments were working continuously due to power outage problems.

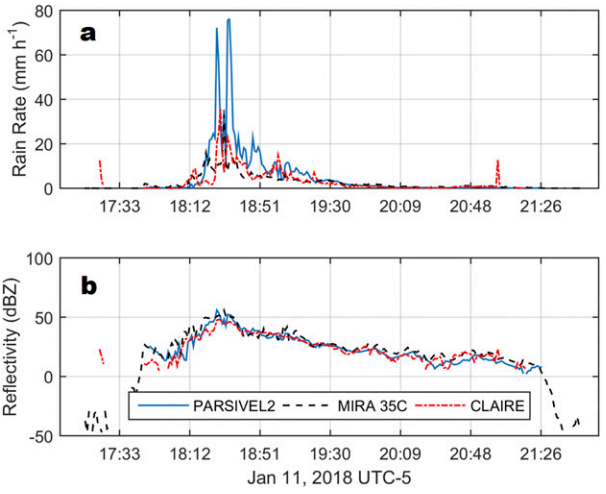

FIG. 9. Comparison of (a) rainfall rate and (b) radar reflectivity factor for the event of 11 Jan 2018. The estimates are made at ranges corresponding to 2 m for PARSIVEL^2, 250 m for MIRA-35c, and 750 m for CLAIRE. The peaks observed in the estimates of rainfall rate coincide with the "spurious mode" observed in Fig. 8 and the attenuation observed in Fig. 7.

Percent bias and percent absolute bias are used to compare the event rain totals between the different instruments. The measurements of the two instruments (x, y) for n samples are calculated as

$$\text{Percent bias} = \frac{\sum_{i=1}^{n}(x_i - y_i)}{\sum_{i=1}^{n}x_i}\times 100\%, \quad (16)$$

$$\text{Percent absolute bias} = \frac{\sum_{i=1}^{n}|x_i - y_i|}{\sum_{i=1}^{n}x_i}\times 100\%, \quad (17)$$

where x is the reference instrument. In this study, the rain gauge CS700 was in operation for all rain events, and it is considered as a reference.

To avoid underestimates caused by data discontinuity, events in which data have not reached 95% of the operating time in minutes were flagged as invalid. This analysis was performed per each instrument.

4. Results

The first step of this work is to validate the relationship between raindrop size (D) and raindrop fall velocity (w_t) [Eq. (5)]. The original formulation of Gunn and Kinzer (1949) was made for particles at sea level. However, the change of air density due to the elevation, like in our study area at 3300 m MSL, has a major influence in the raindrop terminal fall velocity. The Atlas et al. (1973) second-order polynomial approximation of Foote and Du Toit (1969) assumes a U.S. standard atmosphere condition, and it is not representative of conditions in the Peruvian central Andes. The relationship

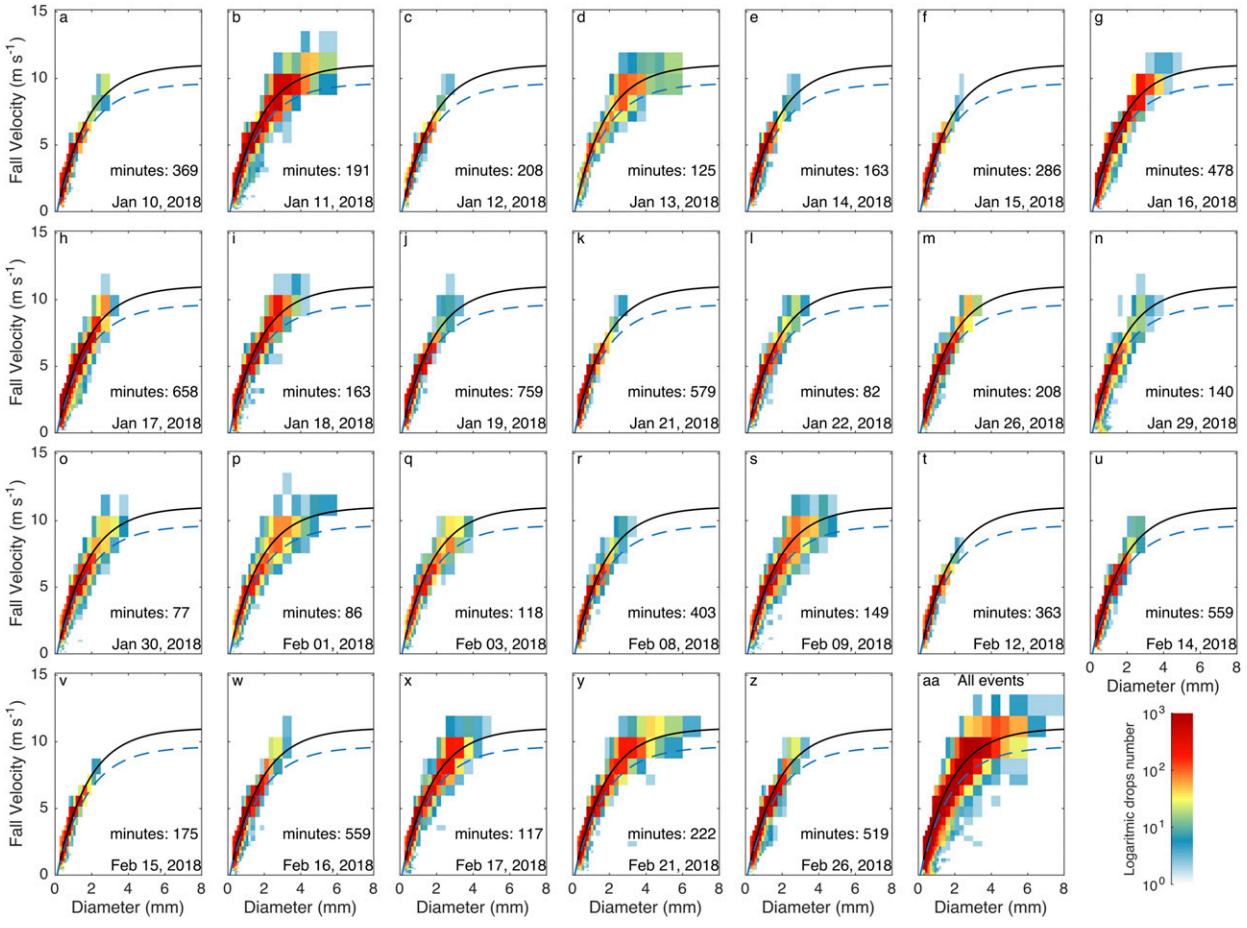

FIG. 10. (a)–(z) Terminal fall velocity as a function of diameter as observed by PARSIVEL^2 for each identified event. (aa) All collected data are shown. The theoretical fall velocity calculated at 3300 m MSL is presented as a black line, while the calculation at sea level is depicted as a blue dashed line. The fall velocity of drops at the Huancayo Observatory's elevation is nearly 15% faster than the one at sea level.

w_t–D measured by PARSIVEL^2, for each of the 27 events considered in the study period, is presented in Fig. 10. The integral number of drops of each event are indicated by the pseudocolor in this paper. The theoretical relationship of diameter and fall velocity with the air density correction of Foote and Du Toit (1969) at 3300 m MSL is depicted in black in comparison to the one at sea level, depicted as a blue dashed line. Theoretically, influence of air density in our study predicts an increase of 15% in the terminal fall velocity with respect to sea level. The 15% represents approximately 1.5 m s^{-1} for drops bigger than 4 mm. The agreement between the theoretical formulation and the observations of drop diameter and terminal fall velocity is consistent with the findings of Bringi et al. (2018). All our cases showed similar behavior, the mean standard error of Eq. (5) for drops smaller than 1 mm is 0.5 m s^{-1}. Only one particular case, drops smaller than 1 mm, had velocities well below the theoretical threshold (Fig. 10n). However, the possible causes still need further investigation. For diameters between 1 and 2 mm, the standard error increase linearly from 0.5 to 1 m s^{-1} and remain constant up to 3 mm of diameter. Between 3 and 6 mm, the standard error could be as high as 1.5 m s^{-1}. Drops larger than 6 mm are scarce and their statistics are not representative.

a. *Raindrop size distribution measurements*

To make the comparison of drops size distribution, the average DSD per event for the MIRA-35c, CLAIRE, and PARSIVEL^2 for 14 events (Fig. 11) are estimated. The closest range gate for each radar is used, which is 250 m for MIRA35c, and 750 m for CLAIRE. There are big differences in the smaller drops (less than 0.5 mm): PARSIVEL^2 shows a decrease in the drop concentration while the radars show an increase. In this study, the better agreement is observed for concentrations for the midsize drop diameters (1–3 mm).

The more noticeable issue in our comparison is that MIRA-35c presents a "spurious mode" in the range of 4–5 mm, which is caused by the effect of the vertical wind velocity (Figs. 8b and 11). At 35 GHz the Mie scattering begins to differ markedly from the Rayleigh scattering at 1 mm of diameter, and again at between 4 and 5 mm the backscattering cross section is drastically reduced and then increases anew (Mie notch). An artificial increase in the number of drops [in the range of 4–5 mm

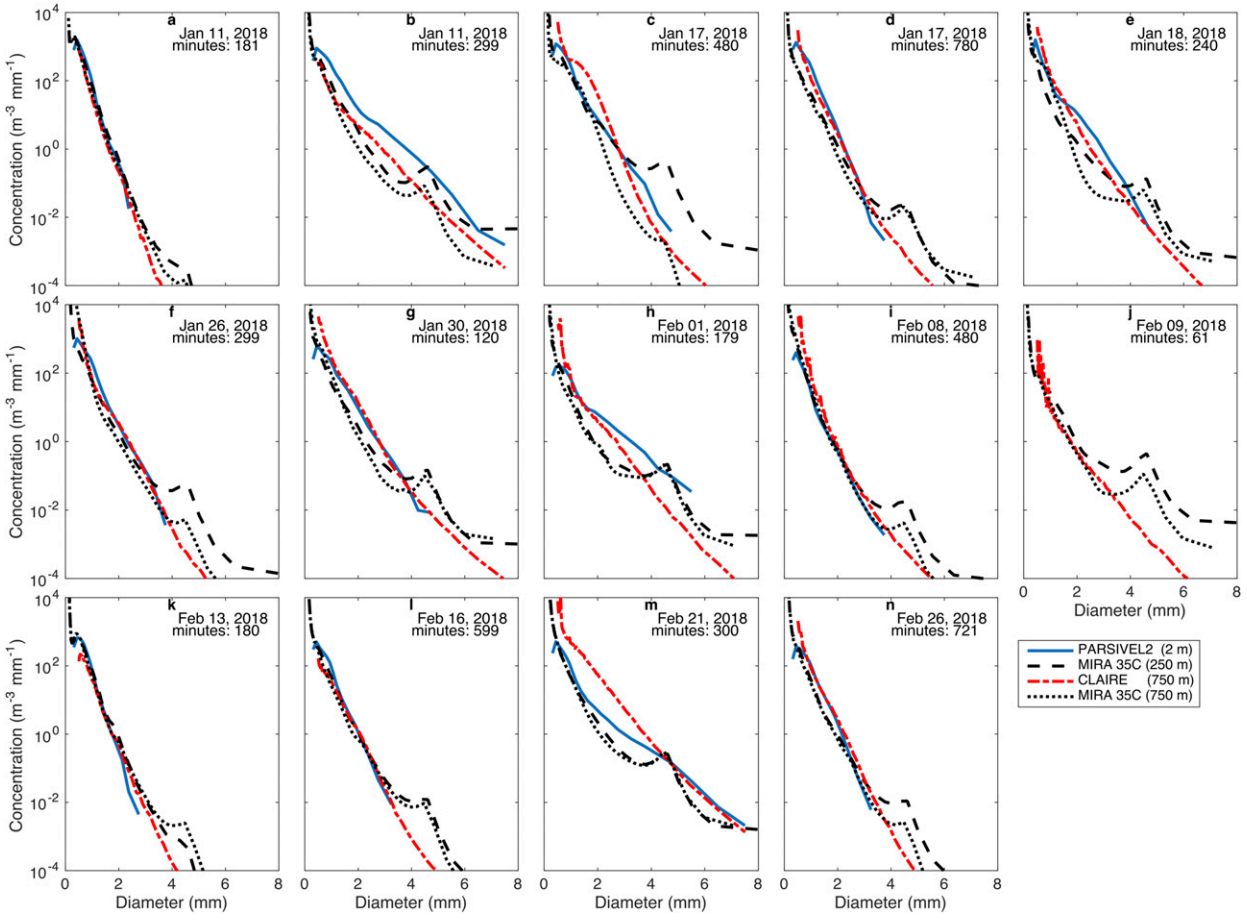

FIG. 11. Mean drop size distribution for each event of studied period. Blue line is for PARSIVEL^2 at 2 m; dashed and dotted black lines are for MIRA-35c at 250 and 750 m, respectively; and dashed–dotted red line is for CLAIRE at 750 m. MIRA-35c estimates present a peak between 4 and 5 mm in most cases, which corresponds to the ''spurious mode.''

derived by Eq. (15)] results from the drops dragged by the updrafts and downdrafts. Since we are using the closest radar gates to the surface from the BLTR, the terminal fall velocity correction of the drops in the MIRA-35c has no effect, because the vertical wind estimates are calculated starting at 500 m AGL. If the DSD at the same height are compared (Fig. 11), the ''spurious mode'' effect was not mitigated as expected. The mode between 4 and 5 mm in the MIRA-35c retrievals is less pronounced, and there is a slight improvement in the concentrations of the larger drops (see Figs. 11a–c,f,i,j,k,n).

For better comparison, the DSD versus time is presented at the same elevation (750 m) for both radars in Figs. 8c and 8d. A correct separation of the fall velocities would have eliminated the ''spurious mode'' that is still noticeable at the MIRA-35c (Fig. 8c) between 1820 and 1840 LT. Additionally, there is significant attenuation at the MIRA-35c during the same period (see Fig. 7a), which affects the DSD estimation.

These results are specially interesting because they show that the separation of the vertical wind velocity and the raindrop terminal fall velocity [Eq. (4)] are not enough to properly estimate the raindrop diameter, especially under convective conditions.

The bias in our methodology might be caused by the negligence of turbulence; in addition, there are considerable differences in the temporal resolution and the sampling volume caused by the different radar beamwidth between MIRA-35c and BLTR, which is another source of error. The clear-air returns from the vertical wind are quite wide as observed in Fig. 5b. Spreading between 0 and $-5\,\mathrm{m\,s^{-1}}$, the mean vertical velocity w for this case is not representative of the real effect in the measured drop velocity. An optimum correction of the raindrop velocity would require the same sampling resolution and temporal averaging between radars. The temporal resolution of BLTR used in this work (32.8 s) seems to be not enough to capture the variability of the updrafts and downdrafts. On the other hand, the 5.6 s of the MIRA-35c temporal resolution seems to be more appropriate for such purpose, but it requires further study.

The effects of wind velocity are hardly noticeable in the drop size distribution of CLAIRE. Due to its frequency and scattering mechanisms, CLAIRE cannot retrieve smaller drops (Fig. 8c), smaller than 0.5 mm. In most cases, the returned signal is contaminated with an interference centered on

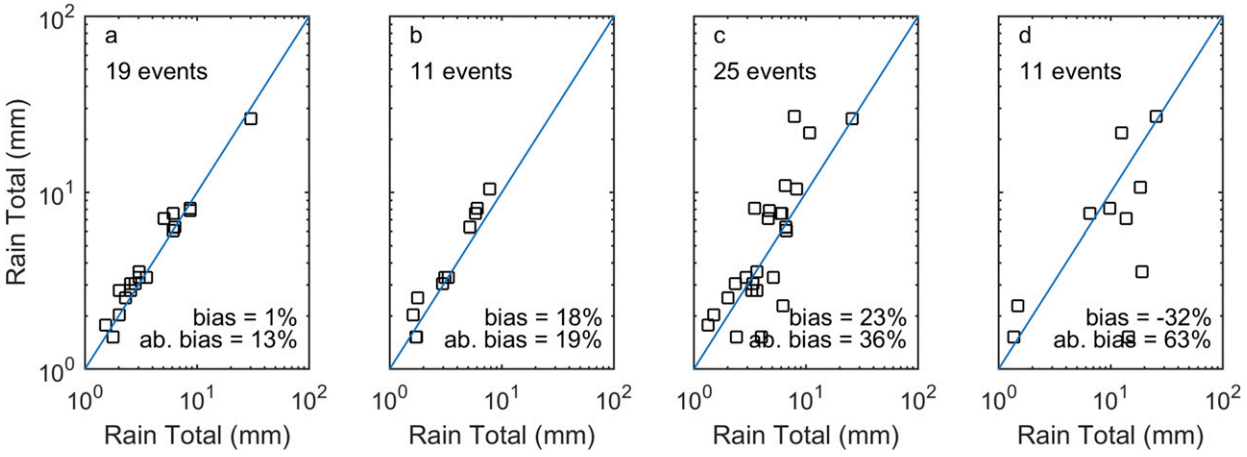

FIG. 12. Comparison of rain event totals (a) between rain gauge 1 and rain gauge 2, (b) between the reference gauge and PARSIVEL^2, (c) between the reference gauge and MIRA-35c, and (d) between the reference gauge and CLAIRE. The estimates are made at ranges corresponding to 2 m for PARSIVEL^2, 250 m for MIRA-35c, and 750 m for CLAIRE.

0 m s^{-1}, which can generate an artificial increase in the drop concentration (Figs. 11h,k,i).

b. Quantitative precipitation estimation

We compare the precipitation estimates from different instruments, integrating the accumulated precipitation of each event. The event definition and metrics are described in section 3c. Not all instruments recorded the same number of events due to power outage during electrical storm, which are common in the region of study. MIRA-35c was the only instrument that operating without interruption during the study period due to its energy autonomy (solar panel and generator set).

The bias between both gauges (Fig. 12a) was 1% and the absolute bias was 13%, indicating the high level of agreement between them. PARSIVEL^2 had 18% of bias with respect to reference gauge and 19% of absolute bias. There is a general underestimation in the PARSIVEL^2's rain totals whose causes are unknown. Tokay et al. (2014) found an overestimation of 4% with respect to a gauge, which should be expected due to the sensitivity of the instrument.

MIRA-35c had a bias of 23% and an absolute bias of 36% (Fig. 12c). Probably the biggest source of underestimation on MIRA-35c is the attenuation from wet antenna (Mandeep 2009), in addition to the difficulty of raindrop size distribution retrieval due to turbulence and Mie scattering.

CLAIRE had −32% of bias and 63% of absolute bias (Fig. 12d). CLAIRE is the instrument with the most discrepancies in the rain totals, despite the fact that the drops size distribution retrieval seems to be better represented than by MIRA-35c. A deeper analysis in the CLAIRE data led us to conclude that the fluctuations in the transmission power clearly affect the estimation of radar reflectivity, which can be easily observed in the events of 1 and 21 February and results in an underestimation and overestimation of drops concentration (Figs. 11h,m).

Estimate comparison between MIRA-35c and CLAIRE (Fig. 13), using MIRA-35c as reference, showed a bias of −168% and 175% in the absolute bias. These results suggest that a real-time calibration is necessary to achieve better estimates of precipitation.

Ground measurements obtained by the disdrometer should be used in order to obtain a more precise calibration of the profiling radar, as suggested by Williams (2009). For the time being, the use of MIRA-35c and CLAIRE for quantitative precipitation estimation (QPE) studies on the ground are not recommended, especially in long-term estimations. This does not rule out the usefulness of these instruments for microphysics studies and microscale process, especially at higher altitudes.

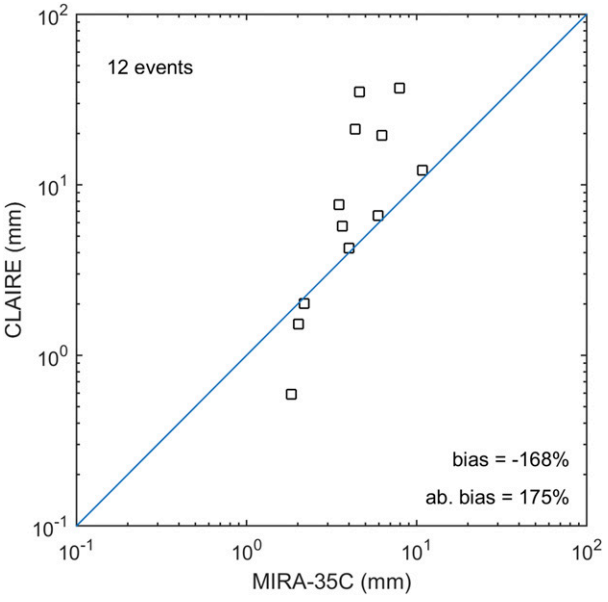

FIG. 13. Comparison of range event totals between MIRA-35c and CLAIRE. The limited number of matching events might be the cause for the high bias (−168%) observed in the comparison.

5. Conclusions

In this work, multiple instruments are used to evaluate their ability to estimate not only rainfall rate, but also their advantages and disadvantages for different precipitation studies. The instruments used in this work consist of two rain gauges and a disdrometer (PARSIVEL^2) for ground measurements, a Ka-band cloud profiler (MIRA-35c), a UHF wind profiler (CLAIRE), and a VHF wind profiler (BLTR). CLAIRE was entirely designed and constructed in the technological development facilities of the Instituto Geofísico del Perú, and in this study the accuracy of rainfall-rate estimates are validated by comparing them with the ones obtained by other instruments. The experimental campaign was carried out in the central Andes (12°S), at the Huancayo Observatory at 3300 m MSL. Based on previous precipitation estimate studies with profilers, we propose in this work a combination of radar observations to reduce the uncertainty generated by the relationship between raindrop diameter and fall velocity. We used the wind vertical velocity measured by VHF wind profiler, BLTR, to correctly separate it from the raindrop terminal fall velocity. Echo separation from hydrometeor and clear air are done from the spectra of CLAIRE and BLTR. The separation algorithm also helped in the removal of the clutter and interference observed in the spectra of both radars. We assessed the Gunn and Kinzer (1949) equation that relates the raindrop diameter and fall velocity, and we used Foote and Du Toit (1969) to correct changes of air density with altitude in the raindrops terminal velocity.

Our observations made with PARSIVEL^2 indicate that the theoretical relationship of raindrop diameter and terminal velocity fit well enough. The standard error of Eq. (5) goes from 0.5 m s^{-1} for the smaller diameters to 1.5 m s^{-1} for diameters within the 6 mm. Drops larger than 6 mm are scarce, and their statistics are not representative. Despite the low bias of the Gunn and Kinzer (1949) equation relationship, MIRA-35c shows a ''spurious mode'' between diameters of 4–5 mm, which are given by the first minimum in the backscattering cross sections at 35 GHz, and the terminal fall velocity correction was not able to mitigate it. These results show that the correction made by using the vertical wind velocity into the raindrop terminal fall velocity is not enough to properly estimate the raindrop diameter, especially under convective conditions and at lower elevations. The bias in our methodology must lie in the assumption of negligible turbulence; in addition, there are considerably differences in the temporal resolution and the sampling volume between MIRA-35c and BLTR, which might be an additional source of errors. An optimum correction of the raindrop velocity would require the same sampling resolution and temporal resolution among radars. The temporal resolution of BLTR used in this work (32.8 s) seems to be not enough to capture the variability of the updrafts and downdrafts. On the other hand, the 5.6 s of the MIRA-35c temporal resolution seems to be more appropriate for such purpose.

The possible causes for discrepancies in precipitation retrievals obtained from CLAIRE are as follows:

1) Smaller drops than 0.5 mm are not detected by the radar, and it is attributed to the radar wavelength.
2) In some cases the spectra is contaminated by an interference centered on 0 m s^{-1}, which can generate an artificial increase in the drop concentration.
3) There are fluctuations in the transmission power which causes changes in the radar calibration constant, and it results in an underestimation and overestimation of drops concentration.

The biases of the PARSIVEL^2, MIRA-35c, and CLAIRE were 18%, 23%, and −32%, respectively, and their respective absolute biases were 19%, 36%, and 63%. There are a general underestimation in the PARSIVEL^2's rain totals that require further investigation. The ground based observation by disdrometer is an option to calibrate the profiling radar more precisely, as is suggested by Williams (2009). For the time being, studies of QPE using MIRA-35c and CLAIRE are not suitable, especially in long-term estimations, because their first valid range from where the estimates are obtained, is not at the ground level. However, this does not rule out the usefulness of these instruments for microphysics and microscale process studies.

Acknowledgments. The authors thank the personnel of the Instituto Geofísico del Perú at Jicamarca Radio Observatory and at Huancayo Observatory for their support during the development of this project. This research is partially funded by INNÓVATE PERÚ (387-PNICP-PIAP-2014). The Jicamarca Radio Observatory is a facility of the Instituto Geofísico del Perú operated with the support from the NSF AGS-1433968 through Cornell University.

REFERENCES

Atlas, D., 1964: Advances in radar meteorology. *Advances in Geophysics*, Vol. 10, Academic Press, 317–478, https://doi.org/10.1016/S0065-2687(08)60009-6.

——, R. C. Srivastava, and R. S. Sekhon, 1973: Doppler radar characteristics of precipitation at vertical incidence. *Rev. Geophys.*, **11**, 1–35, https://doi.org/10.1029/RG011i001p00001.

Barrett, B. S., R. Garreaud, and M. Falvey, 2009: Effect of the Andes Cordillera on precipitation from a midlatitude cold front. *Mon. Wea. Rev.*, **137**, 3092–3109, https://doi.org/10.1175/2009MWR2881.1.

Beard, K. V., 1977: Terminal velocity adjustment for cloud and precipitation drops aloft. *J. Atmos. Sci.*, **34**, 1293–1298, https://doi.org/10.1175/1520-0469(1977)034<1293:TVAFCA>2.0.CO;2.

Bezvesilniy, O., G. Peters, and D. Vavriv, 2013: Estimating cloud and rain parameters from Doppler radar data. *Radio Phys. Radio Astron.*, **8**, 296.

Bohren, C. F., and D. R. Huffman, 1998: *Absorption and Scattering of Light by Small Particles*. Wiley-VCH Verlag, 530 pp., https://doi.org/10.1002/9783527618156.

Briggs, B. H., 1984: The analysis of spaced sensor records by correlation techniques. *Middle Atmosphere Program*, R. Vincent, Ed., Vol. 13, University of Illinois, 166–186.

——, and R. A. Vincent, 1992: Spaced-antenna analysis in the frequency domain. *Radio Sci.*, **27**, 117–129, https://doi.org/10.1029/91RS03051.

Bringi, V., and V. Chandrasekar, 2001: *Polarimetric Doppler Weather Radar: Principles and Applications*. Cambridge University Press, 639 pp.

——, M. Thurai, and D. Baumgardner, 2018: Raindrop fall velocities from an optical array probe and 2-D video disdrometer. *Atmos. Meas. Tech.*, **11**, 1377–1384, https://doi.org/10.5194/amt-11-1377-2018.

Das, S., and A. Maitra, 2016: Vertical profile of rain: Ka band radar observations at tropical locations. *J. Hydrol.*, **534**, 31–41, https://doi.org/10.1016/j.jhydrol.2015.12.053.

——, A. K. Shukla, and A. Maitra, 2010: Investigation of vertical profile of rain microstructure at Ahmedabad in Indian tropical region. *Adv. Space Res.*, **45**, 1235–1243, https://doi.org/10.1016/j.asr.2010.01.001.

——, A. Maitra, and A. K. Shukla, 2011a: Melting layer characteristics at different climatic conditions in the Indian region: Ground based measurements and satellite observations. *Atmos. Res.*, **101**, 78–83, https://doi.org/10.1016/j.atmosres.2011.01.013.

——, S. Talukdar, A. Bhattacharya, A. Adhikari, and A. Maitra, 2011b: Vertical profile of Z-R relationship and its seasonal variation at a tropical location. *2011 IEEE Applied Electromagnetics Conf.*, Kolkata, India, IEEE, 18–22, https://doi.org/10.1109/AEMC.2011.6256915.

Derin, Y., and Coauthors, 2016: Multiregional satellite precipitation products evaluation over complex terrain. *J. Hydrometeor.*, **17**, 1817–1836, https://doi.org/10.1175/JHM-D-15-0197.1.

Doviak, R. J., and D. S. Zrnić, 1984: *Doppler Radar and Weather Observations*. 2nd ed. Vol. 33, Elsevier, 545 pp., https://doi.org/10.1016/B978-0-12-221422-6.50022-X.

Ellis, S. M., and J. Vivekanandan, 2011: Liquid water content estimates using simultaneous S and K_a band radar measurements. *Radio Sci.*, **46**, RS2021, https://doi.org/10.1029/2010RS004361.

Firda, J. M., S. M. Sekelsky, and R. E. McIntosh, 1999: Application of dual-frequency millimeter-wave Doppler spectra for the retrieval of drop size distributions and vertical air motion in rain. *J. Atmos. Oceanic Technol.*, **16**, 216–236, https://doi.org/10.1175/1520-0426(1999)016<0216:AODFMW>2.0.CO;2.

Foote, G. B., and P. S. Du Toit, 1969: Terminal velocity of raindrops aloft. *J. Appl. Meteor.*, **8**, 249–253, https://doi.org/10.1175/1520-0450(1969)008<0249:TVORA>2.0.CO;2.

Giangrande, S. E., E. P. Luke, and P. Kollias, 2012: Characterization of vertical velocity and drop size distribution parameters in widespread precipitation at ARM facilities. *J. Appl. Meteor. Climatol.*, **51**, 380–391, https://doi.org/10.1175/JAMC-D-10-05000.1.

Gunn, R., and G. D. Kinzer, 1949: The terminal velocity of fall for water droplets in stagnant air. *J. Meteor.*, **6**, 243–248, https://doi.org/10.1175/1520-0469(1949)006<0243:TTVOFF>2.0.CO;2.

Hildebrand, P. H., and R. S. Sekhon, 1974: Objective determination of the noise level in Doppler spectra. *J. Appl. Meteor.*, **13**, 808–811, https://doi.org/10.1175/1520-0450(1974)013<0808:ODOTNL>2.0.CO;2.

Hou, A. Y., and Coauthors, 2014: The Global Precipitation Measurement Mission. *Bull. Amer. Meteor. Soc.*, **95**, 701–722, https://doi.org/10.1175/BAMS-D-13-00164.1.

Junquas, C., K. Takahashi, T. Condom, J.-C. Espinoza, S. Chavez, J.-E. Sicart, and T. Lebel, 2018: Understanding the influence of orography on the precipitation diurnal cycle and the associated atmospheric processes in the central Andes. *Climate Dyn.*, **50**, 3995–4017, https://doi.org/10.1007/s00382-017-3858-8.

Kneifel, S., P. Kollias, A. Battaglia, J. Leinonen, M. Maahn, H. Kalesse, and F. Tridon, 2016: First observations of triple-frequency radar Doppler spectra in snowfall: Interpretation and applications. *Geophys. Res. Lett.*, **43**, 2225–2233, https://doi.org/10.1002/2015GL067618.

Kollias, P., B. A. Albrecht, and F. Marks Jr., 2002: Why Mie? Accurate observations of vertical air velocities and raindrops using a cloud radar. *Bull. Amer. Meteor. Soc.*, **83**, 1471–1484, https://doi.org/10.1175/BAMS-83-10-1471.

——, ——, and ——, 2003: Cloud radar observations of vertical drafts and microphysics in convective rain. *J. Geophys. Res.*, **108**, 4053, https://doi.org/10.1029/2001JD002033.

——, E. E. Clothiaux, M. A. Miller, B. A. Albrecht, G. L. Stephens, and T. P. Ackerman, 2007: Millimeter-wavelength radars: New frontier in atmospheric cloud and precipitation research. *Bull. Amer. Meteor. Soc.*, **88**, 1608–1624, https://doi.org/10.1175/BAMS-88-10-1608.

——, N. Bharadwaj, K. Widener, I. Jo, and K. Johnson, 2014: Scanning ARM cloud radars. Part I: Operational sampling strategies. *J. Atmos. Oceanic Technol.*, **31**, 569–582, https://doi.org/10.1175/JTECH-D-13-00044.1.

Lewis, B. L., and F. F. Kretschmer, 1982: Linear frequency modulation derived polyphase pulse compression codes. *IEEE Trans. Aerosp. Electron. Syst.*, **18**, 637–641, https://doi.org/10.1109/TAES.1982.309276.

Lhermitte, R. M., 1988: Observation of rain at vertical incidence with a 94 GHz Doppler radar: An insight on Mie scattering. *Geophys. Res. Lett.*, **15**, 1125–1128, https://doi.org/10.1029/GL015i010p01125.

Löffler-Mang, M., and J. Joss, 2000: An optical disdrometer for measuring size and velocity of hydrometeors. *J. Atmos. Oceanic Technol.*, **17**, 130–139, https://doi.org/10.1175/1520-0426(2000)017<0130:AODFMS>2.0.CO;2.

Maahn, M., and P. Kollias, 2012: Improved micro rain radar snow measurements using Doppler spectra post-processing. *Atmos. Meas. Tech.*, **5**, 2661–2673, https://doi.org/10.5194/amt-5-2661-2012.

Mandeep, J. S., 2009: Analysis effect of water on a Ka-band antenna. *Prog. Electromagn. Res. Lett.*, **9**, 49–57, https://doi.org/10.2528/PIERL09041604.

Mantas, V. M., Z. Liu, C. Caro, and A. J. S. C. Pereira, 2015: Validation of TRMM Multi-Satellite Precipitation Analysis (TMPA) products in the Peruvian Andes. *Atmos. Res.*, **163**, 132–145, https://doi.org/10.1016/j.atmosres.2014.11.012.

Marshal, J. S., and W. M. Palmer, 1948: The dristibution of raindrops with size. *J. Meteor.*, **5**, 165–166, https://doi.org/10.1175/1520-0469(1948)005<0165:TDORWS>2.0.CO;2.

Martínez Grimaldo, A., Y. Silva Vidal, and K. Takahashi, 2005: *Vulnerabilidad actual y futura ante el cambio climático y medidas de adaptación en la Cuenca del rio Mantaro*. Vol. III. Instituto Geofísico del Perú, 106 pp.

McDonald, A. J., T. K. Carey-Smith, D. A. Hooper, G. J. Fraser, and B. P. Lublow, 2004: The effect of precipitation on wind-profiler clear air returns. *Ann. Geophys.*, **22**, 3959–3970, https://doi.org/10.5194/angeo-22-3959-2004.

Mourre, L., T. Condom, C. Junquas, T. Lebel, J. E. Sicart, R. Figueroa, and A. Cochachin, 2016: Spatio-temporal assessment of WRF, TRMM and in situ precipitation data in a tropical mountain environment (Cordillera Blanca, Peru). *Hydrol. Earth Syst. Sci.*, **20**, 125–141, https://doi.org/10.5194/hess-20-125-2016.

Moya-Álvarez, A. S., J. Gálvez, A. Holguín, R. Estevan, S. Kumar, E. Villalobos, D. Martínez-Castro, and Y. Silva, 2018a: Extreme rainfall forecast with the WRF-ARW model in the central Andes of Peru. *Atmosphere*, **9**, 362, https://doi.org/10.3390/atmos9090362.

——, D. Martínez-Castro, J. L. Flores, and Y. Silva, 2018b: Sensitivity study on the influence of parameterization schemes in WRF-ARW model on short- and medium-range precipitation forecasts in the central Andes of Peru.

Adv. Meteor., **2018**, 1381092, https://doi.org/10.1155/2018/1381092.

——, ——, S. Kumar, R. Estevan, and Y. Silva, 2019: Response of the WRF Model to different resolutions in the rainfall forecast over the complex Peruvian orography. *Theor. Appl. Climatol.*, **137**, 2993–3007, https://doi.org/10.1007/s00704-019-02782-3.

Oscanoa, J., C. Castillo, and D. Scipion, 2016: CLAIRE: An UHF wind profiler radar for turbulence and precipitation studies. *2016 IEEE 23rd Int. Congress on Electronics, Electrical Engineering and Computing*, Piura, Peru, IEEE, https://doi.org/10.1109/INTERCON.2016.7815577.

Peel, M. C., B. L. Finlayson, and T. A. McMahon, 2007: Updated world map of the Köppen-Geiger climate classification. *Hydrol. Earth Syst. Sci.*, **11**, 1633–1644, https://doi.org/10.5194/hess-11-1633-2007.

Peters, G., B. Fischer, and T. Andersson, 2002: Rain observations with a vertically looking micro rain radar (MRR). *Boreal Environ. Res.*, **7**, 353–362.

——, ——, H. Münster, M. Clemens, and A. Wagner, 2005: Profiles of raindrop size distributions as retrieved by microrain radars. *J. Appl. Meteor.*, **44**, 1930–1949, https://doi.org/10.1175/JAM2316.1.

——, ——, and M. Clemens, 2010: Rain attenuation of radar echoes considering finite-range resolution and using drop size distributions. *J. Atmos. Oceanic Technol.*, **27**, 829–842, https://doi.org/10.1175/2009JTECHA1342.1.

Pfitzenmaier, L., A. Battaglia, and P. Kollias, 2019: The impact of the radar-sampling volume on multiwavelength spaceborne radar measurements using airborne radar observations. *Remote Sens.*, **11**, 2263, https://doi.org/10.3390/rs11192263.

Ralph, F. M., 1995: Using radar-measured radial vertical velocities to distinguish precipitation scattering from clear-air scattering. *J. Atmos. Oceanic Technol.*, **12**, 257–267, https://doi.org/10.1175/1520-0426(1995)012<0257:URMRVV>2.0.CO;2.

Schafer, R., S. Avery, P. May, D. Rajopadhyaya, and C. Williams, 2002: Estimation of rainfall drop size distributions from dual-frequency wind profiler spectra using deconvolution and a nonlinear least squares fitting technique. *J. Atmos. Oceanic Technol.*, **19**, 864–874, https://doi.org/10.1175/1520-0426(2002)019<0864:EORDSD>2.0.CO;2.

Scheel, M. L. M., M. Rohrer, C. Huggel, D. Santos Villar, E. Silvestre, and G. J. Huffman, 2011: Evaluation of TRMM Multi-Satellite Precipitation Analysis (TMPA) performance in the central Andes region and its dependency on spatial and temporal resolution. *Hydrol. Earth Syst. Sci.*, **15**, 2649–2663, https://doi.org/10.5194/hess-15-2649-2011.

Tokay, A., D. B. Wolff, and W. A. Petersen, 2014: Evaluation of the new version of the laser-optical disdrometer, OTT PARSIVEL^2. *J. Atmos. Oceanic Technol.*, **31**, 1276–1288, https://doi.org/10.1175/JTECH-D-13-00174.1.

Tridon, F., and A. Battaglia, 2015: Dual-frequency radar doppler spectral retrieval of rain drop size distributions and entangled dynamics variables. *J. Geophys. Res. Atmos.*, **120**, 5585–5601, https://doi.org/10.1002/2014JD023023.

——, ——, E. Luke, and P. Kollias, 2017: Rain retrieval from dual-frequency radar Doppler spectra: Validation and potential for a midlatitude precipitating case-study. *Quart. J. Roy. Meteor. Soc.*, **143**, 1364–1380, https://doi.org/10.1002/qj.3010.

——, and Coauthors, 2019: The microphysics of stratiform precipitation during OLYMPEX: Compatibility between triple-frequency radar and airborne in situ observations. *J. Geophys. Res. Atmos.*, **124**, 8764–8792, https://doi.org/10.1029/2018JD029858.

Valdivia, J. M., 2018: Cuantificación de lluvias usando el radar perfilador de banda Ka MIRA 35c. B.S. thesis, Universidad Nacional José Faustino Sánchez Carrión, 95 pp.

——, K. Contreras, D. Martinez-Castro, E. Villalobos-Puma, L. F. Suarez-Salas, and Y. Silva, 2020: Dataset on raindrop size distribution, raindrop fall velocity and precipitation data measured by disdrometers and rain gauges over Peruvian central Andes (12.0°S). *Data Brief*, **29**, 105215, https://doi.org/10.1016/j.dib.2020.105215.

Viale, M., and F. A. Norte, 2009: Strong cross-barrier flow under stable conditions producing intense winter orographic precipitation: A case study over the subtropical central Andes. *Wea. Forecasting*, **24**, 1009–1031, https://doi.org/10.1175/2009WAF2222168.1.

Welch, P. D., 1967: The use of fast Fourier transform for the estimation of power spectra: A method based on time averaging over short, modified periodograms. *IEEE Trans. Audio Electroacoust.*, **15**, 70–73, https://doi.org/10.1109/TAU.1967.1161901.

Williams, C. R., 2002: Simultaneous ambient air motion and raindrop size distributions retrieved from UHF vertical incident profiler observations. *Radio Sci.*, **37**, 1024, https://doi.org/10.1029/2000RS002603.

——, 2009: Accuracy of reflectivity estimated from profiling radars. *2009 IEEE Radar Conf.*, Pasadena, CA, IEEE, https://doi.org/10.1109/RADAR.2009.4976996.

——, W. L. Ecklund, and K. S. Gage, 1995: Classification of precipitating clouds in the tropics using 915-MHz wind profilers. *J. Atmos. Oceanic Technol.*, **12**, 996–1012, https://doi.org/10.1175/1520-0426(1995)012<0996:COPCIT>2.0.CO;2.

——, M. Maahn, J. C. Hardin, and G. D. Boer, 2018: Clutter mitigation, multiple peaks, and high-order spectral moments in 35-GHz vertically pointing radar velocity spectra. *Atmos. Meas. Tech.*, **11**, 4963–4980, https://doi.org/10.5194/amt-11-4963-2018.

Williams, J. K., and J. Vivekanandan, 2007: Sources of error in dual-wavelength radar remote sensing of cloud liquid water content. *J. Atmos. Oceanic Technol.*, **24**, 1317–1336, https://doi.org/10.1175/JTECH2042.1.